Original Article

Diagnostic value of single-source dual-energy spectral computed tomography in differentiating parotid gland tumors: initial results

Lin Li[1#], Yanfeng Zhao[1#], Dehong Luo[1], Liang Yang[2], Lei Hu[1], Xinming Zhao[1], Yong Wang[3], Wensheng Liu[4]

[1]Department of Diagnostic Radiology, National Cancer Center/National Clinical Research Center for Cancer/Cancer Hospital, Chinese Academy of Medical Sciences and Peking Union Medical College, Beijing 100021, China; [2]Department of Diagnostic Radiology, Beijing Chaoyang Hospital, Capital Medical University, Beijing 100020, China; [3]Department of Ultrasonography, [4]Department of Head and Neck Surgery, National Cancer Center/National Clinical Research Center for Cancer/Cancer Hospital, Chinese Academy of Medical Sciences and Peking Union Medical College, Beijing 100021, China

[#]These authors contributed equally to this work.

Correspondence to: Wensheng Liu. Department of Head and Neck Surgery, National Cancer Center/National Clinical Research Center for Cancer/Cancer Hospital, Chinese Academy of Medical Sciences and Peking Union Medical College, No. 17, Panjiayuannanli, Chaoyang District. Beijing 100021, China. Email: lwsdoct@aliyun.com; Dehong Luo. Department of Diagnostic Radiology, National Cancer Center/National Clinical Research Center for Cancer/Cancer Hospital, Chinese Academy of Medical Sciences and Peking Union Medical College, No. 17, Panjiayuannanli, Chaoyang District. Beijing 100021, China. Email: luodehong@163.com; Yong Wang. Department of Ultrasonography, National Cancer Center/National Clinical Research Center for Cancer/Cancer Hospital, Chinese Academy of Medical Sciences and Peking Union Medical College, No. 17, Panjiayuannanli, Chaoyang District. Beijing 100021, China. Email: drwangyong77@163.com.

Background: An accurate preoperative diagnosis that helps distinguish between benign and malignant parotid gland tumors is very important because the results strongly affect surgical procedures. We aimed to evaluate the value of single-source dual-energy computed tomography (ssDECT) in differentiating malignant from benign parotid gland tumors.

Methods: Fifty patients underwent enhanced neck ssDECT scanning before surgery. The images were analyzed using the gemstone spectral imaging (GSI) viewer software.

Results: Fifty-two tumors (43 patients) were confirmed histopathologically, comprising of 12 pleomorphic adenomas (PAs), 24 Warthin tumors (WTs) (15 patients), and 16 malignant tumors (MTs). The iodine concentration (IC), normalized iodine concentration to common carotid artery (NIC_A) and slope value of the spectral curve (λ_{HU}) of the WTs were significantly higher than those of MTs and PAs (all $P<0.05$). The optimal IC, NIC_A and λ_{HU} thresholds for differentiating PAs from MTs were 0.91 mg/mL, 0.15 and 1.09, respectively, achieving sensitivities of 91.7%, 91.7% and 91.7%, specificities of 95.0%, 85.0% and 95.0%, and accuracies of 94.2%, 86.5% and 94.2%, respectively for distinguishing PAs from MTs. The optimal IC, NIC_A and λ_{HU} thresholds for distinguishing WTs from MTs were 1.46 mg/mL, 0.20 and 1.72, achieving sensitivities of 91.7%, 95.8% and 91.7%, and specificities of 89.3%, 85.7% and 89.3%, respectively. The accuracy was 90.4%, 90.4% and 90.4%, respectively.

Conclusions: The parameters of ssDECT in enhanced CT scans are useful in the differential diagnosis of parotid tumors.

Keywords: Computed tomography (CT); dual-energy; parotid gland tumors

Submitted Jul 08, 2018. Accepted for publication Jul 16, 2018.
doi: 10.21037/qims.2018.07.07
View this article at: http://dx.doi.org/10.21037/qims.2018.07.07

Introduction

Salivary gland tumors account for approximately 3–6% globally and 2% in China of all head and neck tumors (1). The parotid gland is the largest salivary gland. Most parotid tumors present as slow growing, painless masses. An accurate preoperative differential diagnosis between benign and malignant tumors (MTs) is very important because the results strongly affect surgical procedures. In patients with benign tumors, the surgical procedure may be limited to superficial parotidectomy, while patients with MTs usually undergo total parotidectomy with possible facial nerve sacrifice. The pathological type of parotid gland tumor is very complex. Fine needle aspiration biopsy (FNAB) is helpful in differentiating a MTs from a benign tumor. However, it is an invasive examination, and has the risk of facial nerve injury (2). Therefore, noninvasive imaging is very important for differential diagnosis. Various noninvasive imaging modalities including ultrasound (US), computed tomography (CT), and magnetic resonance imaging (MRI) have been used to diagnose parotid gland tumors. In China, US is widely accepted as the first choice for the assessment of parotid glands tumors. There have been many reports on the differential diagnosis of parotid tumors by US (3,4). However, it is often difficult to scan the deep lobe because of the acoustic shadow of the mandible, and it is not possible to visualize the intracranial or skull base extent of the mass, and the results are closely related to the operator's experience. MRI is a good choice for evaluation of suspected parotid gland tumors. It can clearly identify not only the tumor's location and extent, but also its relationship with adjacent structures. Some studies reported that dynamic contrast-enhanced MRI (DCE-MRI) and intravoxel incoherent motion (IVIM) were useful in the differential diagnosis of parotid gland tumors (5-8). Nevertheless, its shortcomings are limited availability, high cost and long examination time. Previous CT imaging studies were focused on morphological characteristics such as margin, size, location, density and enhancement patterns. Several studies have investigated the value of dual- or multi-phase CT and CT perfusion in differentiating malignant parotid gland tumors from benign tumors (9-11). They found that the percentage washout ratios in contrast material-enhanced CT may reflect various characters of parotid gland tumors and assist in differentiating benign from MTs (9-11). However, conventional enhanced CT scanning can only provide two or multi-phase enhanced patterns of the lesions and it does not provide quantification parameters in parotid gland lesions.

Recently, a new single-source dual-energy computed tomography (ssDECT) technology was introduced, which uses dual energy x-rays produced by the rapid switching between 80 and 140 kVp within a rotation. It creates both material decomposition (MD) images (e.g., iodine and water-based MD images) and monochromatic spectral images, with energies ranging from 40 to 140 keV. The MD images can be used to estimate quantitatively the iodine concentration (IC) and water concentration (WC) in lesions and normal tissues (12,13). The spectral HU curve can be acquired using spectral CT. Several studies have shown that DECT scanning has significant potential in differentiating MTs from benign tumors in the lungs, liver, pancreas, thyroid and so on (14-20). Previous study has shown that spectral CT texture analysis with machine learning for tissue classification contributes to improved diagnostic accuracy (21). However, to our knowledge, no previous study has discussed the differentiation of parotid gland tumors with the parameters from DECT. Therefore, the purpose of our study was to quantitatively evaluate the diagnostic value of single-source dual-energy spectral CT in the differential diagnosis of parotid gland tumors (3).

Methods

Patients

The study was approved by the Ethics Committee of our hospital and all patients were provided with written informed consent. Our inclusion criteria were as follows: (I) primary parotid gland tumor; (II) no contrast agent allergy; (III) no other MTs in the body. Fifty patients with suspected parotid tumors underwent DECT before surgery from January 2014 to January 2017. All patients underwent surgery after the imaging diagnosis and the final diagnosis was made by histopathological examination.

Imaging technique

All patients were scanned using a GE Discovery CT750 HD scanner (Discovery CT750 HD; GE Healthcare, Milwaukee, WI, USA) using the single-source, dual-energy gemstone spectral imaging (GSI) mode with a fast tube voltage switching between 80 and 140 kVp. The scanning range was from the skull base to the thoracic inlet. The scanning parameters were as follows: thickness, 0.625 mm; tube current fix at 260 mA; rotation speed, 0.7 seconds per rotation, helical pitch, 0.984. All patients received a total of 90 mL of non-ionic contrast agent (300 mgI/mL; Ultravist™; Bayer, Germany) at a rate of 3 mL/s using a power injector. The delay time was 45 s after injection. Before the scan, the patients were asked to take off any false teeth and not to swallow to limit laryngeal motion.

Image analysis

Image processing and analysis were performed using GSI Viewer software 4.6 (GE Healthcare). The default 70 keV monochromatic images and MD images (iodine- and water-based) were reviewed. The number of lesions and their anatomic information including site, location and size were observed and measured. The quantitative spectral CT imaging parameters (CT value, IC, WC) were measured by one radiologist (Lin Li). Circular or oval regions of interest (ROIs) were placed on the lesion, normal parotid, common carotid arteries (CCA) and sternocleidomastoid muscles on the default 70 keV monochromatic images. The ROIs encompassed as much of the lesions as possible and carefully avoided the calcifications and obvious vessels. All measurements were performed three times at different image levels centered on the lesion, and average values were calculated. The GSI viewer software automatically propagated the IC, WC measurements for the lesions, parotid and CCA. One parameter was derived from the IC measurements: normalized iodine concentration (NIC) to CCA, calculated as normalized iodine concentration to common carotid artery (NIC_A)= IC_{lesion}/IC_{CCA}, where IC_{lesion} and IC_{CCA} are the ICs in lesions and in CCA, respectively. The slope of spectral curves (λ_{HU}) was calculated by using the following equation: $\lambda_{HU} = (HU_{40keV} - HU_{100keV})/(100-40)$.

Statistical analyses

All statistical analyses were performed with the SPSS 13.0 (SPSS Inc., Chicago, IL, USA) statistical software package. Quantitative data are presented as means ± standard deviations (X ± S). The normality and homogeneity of variance among all measurement data were analyzed by using one-way analysis of variance ANOVA, and an inter-group comparison was performed with the least significant difference (LSD) method. A value of P>0.05 indicated no statistically significant difference. The diagnostic capability was determined by calculating the area under the receiver operating characteristic (ROC) curve. The best sensitivity and specificity were achieved by using the optimal thresholds. The null hypothesis test was that the area under the ROC curve was 0.5.

Results

General information

In 50 patients, seven patients (14.0%) were excluded from this study because of (I) inadequate confirmation of histologic findings (n=4); (II) pure cystic mass (n=1); and (III) inflammatory masses (n=2). Therefore, 43 patients (32 men, 11 women; age range, 26–78 years; mean age, 52.6 years) with 52 tumors were finally included in our study, which comprised 12 pleomorphic adenomas (PAs), 24 Warthin tumors (WTs) (15 patients), and 16 MTs (4 mucoepidermoid carcinomas, 4 squamous cell carcinoma, 3 duct cell carcinoma, 2 acinic cell carcinomas, 2 lymphomas, and 1 carcinoma ex PA) diagnosed by pathological examination after surgery with the mean longest diameter of 2.53 (0.9–8.9) cm, and the mean shortest diameter of 2.05 (0.6–7.8) cm. In patients with WTs, five patients had two tumors, and two had three tumors, all the tumors were assessed.

The patients' general information of different pathological types in parotid gland is listed in *Table 1*.

Spectral CT parameters in different pathologies

The average values of spectral CT parameters for different pathological entities of the parotid gland are listed in *Table 2*.

According to *Table 2*, there were significant differences in the IC, WC, NIC_A and λ_{HU} among the 3 groups (P<0.05), and the IC, NIC_A and λ_{HU} were highest in WT, followed by MT and PA (*Figures 1-4*). An inter-group comparison was performed with the LSD method. The results are as follows: there were significant differences in the IC, NIC_A and λ_{HU} between every two groups. Comparisons of the WC demonstrated a significant difference only between the PA group and the WT group. Therefore, we chose three parameters in our study: IC, NIC_A and λ_{HU} for performing the ROC study.

Table 3 shows the thresholds and diagnostic efficacies of spectral CT parameters for the differential diagnosis.

The results showed that the optimal IC, NIC_A and λ_{HU} thresholds were 0.91 mg/mL, 0.15 and 1.09, respectively for differentiating PAs from MTs, achieving sensitivities of 91.7%, 91.7% and 91.7%, specificities of 95.0%, 85.0% and 95.0%, and accuracies of 94.2%, 86.5% and 94.2%,

Table 1 Patients' general information of different pathological types in parotid gland

Findings	PA	WT	MT	P value
Sex (M/F)	7/5	13/2	12/4	0.245
Age	43.5	60.2	52.19	0.006
BMI	24.48±3.61	23.63±2.27	23.93±3.48	0.781
Number (single/multiple)	12/0	8/7	16/0	0.000
Site (R/L)	7/5	15/9	11/5	0.844
Location (S/D)	9/3	17/7	12/4	0.945

For sex, age, BMI and number, the patient number =43; for site and location, the tumor number =52. PA, pleomorphic adenoma; WT, Warthin tumors; MT, malignant tumors; M, male; F, female; BMI, body mass index; R, right; L, left; S, superficial lobe; D, deep lobe.

Table 2 The spectral parameters for different pathological entities of the parotid gland

Group	PA	MT	WT	F	P
IC (mg/mL)	0.59±0.28	1.48±0.90	2.45±0.82	25.397	0.000
WC (mg/mL)	1,027.52±5.56	1,034.31±11.10	1,037.68±9.17	4.904	0.011
NIC_A	0.09±0.05	0.21±0.12	0.33±0.08	28.471	0.000
λ_{HU}	0.64±0.44	1.75±1.08	2.76±0.08	22.23	0.000

PA, pleomorphic adenoma; WT, Warthin tumors; MT, malignant tumors; F, the statistics of ANOVA; IC, iodine concentration; WC, water concentration; NIC_A, normalized iodine concentration to common carotid artery.

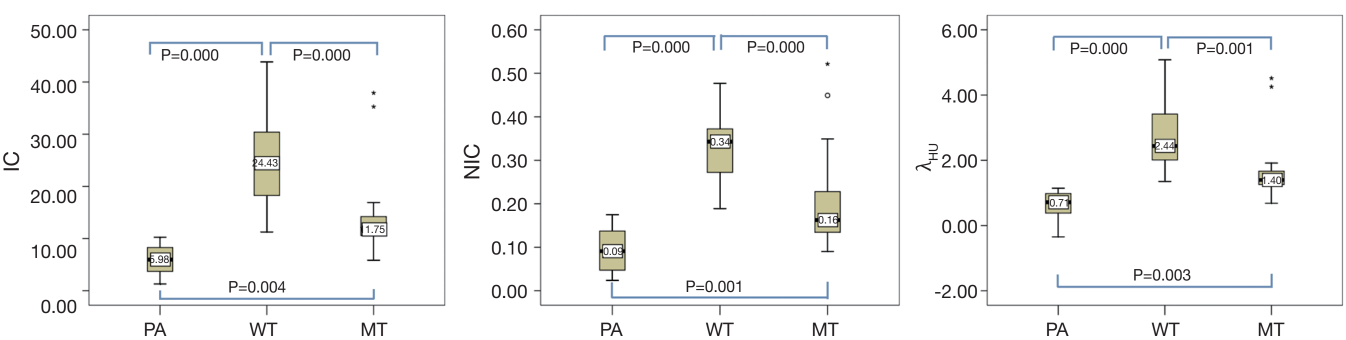

Figure 1 Box plots of IC (A), NIC (B) and λ_{HU} (C) for the 3 groups of tumors. The IC, NIC_A and λ_{HU} of WTs are significantly higher than those of MTs and PAs. Inter-group comparison is performed with the LSD method. IC, iodine concentration; NIC_A, normalized iodine concentration to common carotid artery; WTs, Warthin tumors; MTs, malignant tumors; PAs, pleomorphic adenomas; LSD, least significant difference.

respectively for distinguishing PAs from MTs. The optimal IC, NIC_A and λ_{HU} threshold was 1.46 mg/mL, 0.20 and 1.72, achieving 91.7%, 95.8% and 91.7% sensitivity, 89.3%, 85.7% and 89.3% specificity respectively. The accuracy was 90.4%, 90.4% and 90.4%, respectively for distinguishing WTs from MTs. ROC curves showed that the IC and λ_{HU} have higher diagnostic efficacies than NIC_A in differentiating MT from PA, the area under the curves (AUCs) were 0.943 and 0.943 (*Figure 5A*) and in MT from WT, the AUCs were 0.844 and 0.849 (*Figure 5B*).

Discussion

The precise preoperative diagnosis of parotid gland tumors

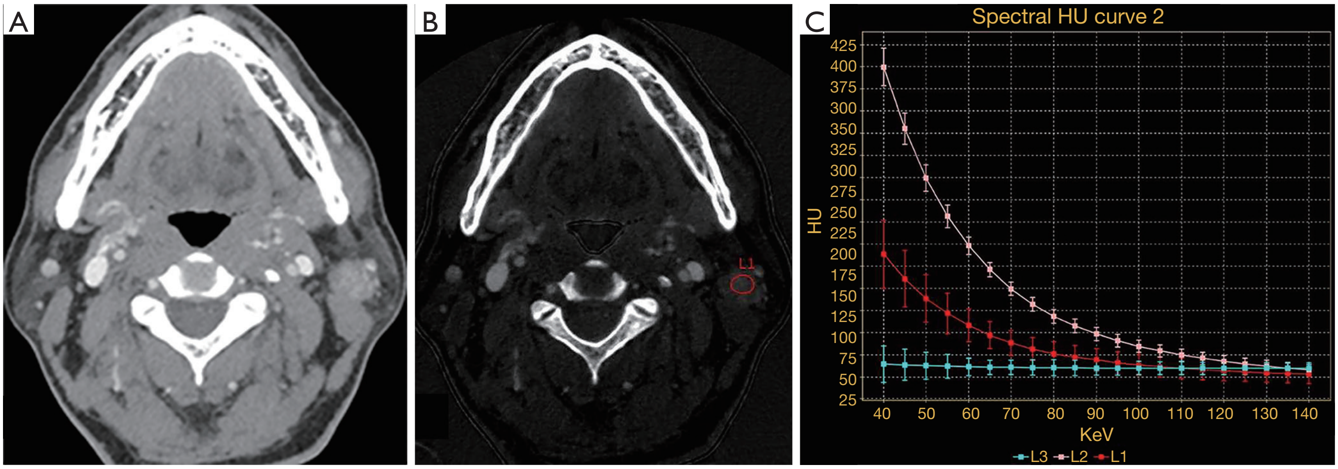

Figure 2 A 50-year-old male patient with WT. (A) Transverse 70 keV images after enhancement. The tumor locates in the left lobe of parotid gland with clear border and marked enhancement; (B) iodine-based MD images and (C) the spectral HU curves are the tumor (L1, the red curve), CCA (L2, the pink curve) and sternocleidomastoid muscle (L3, the blue curve) respectively. The IC, NIC and λ_{HU} are 2.00 mg/mL, 0.48 and 2.37, respectively. WT, Warthin tumor; MD, material decomposition; CCA, common carotid arteries; IC, iodine concentration; NIC, normalized iodine concentration.

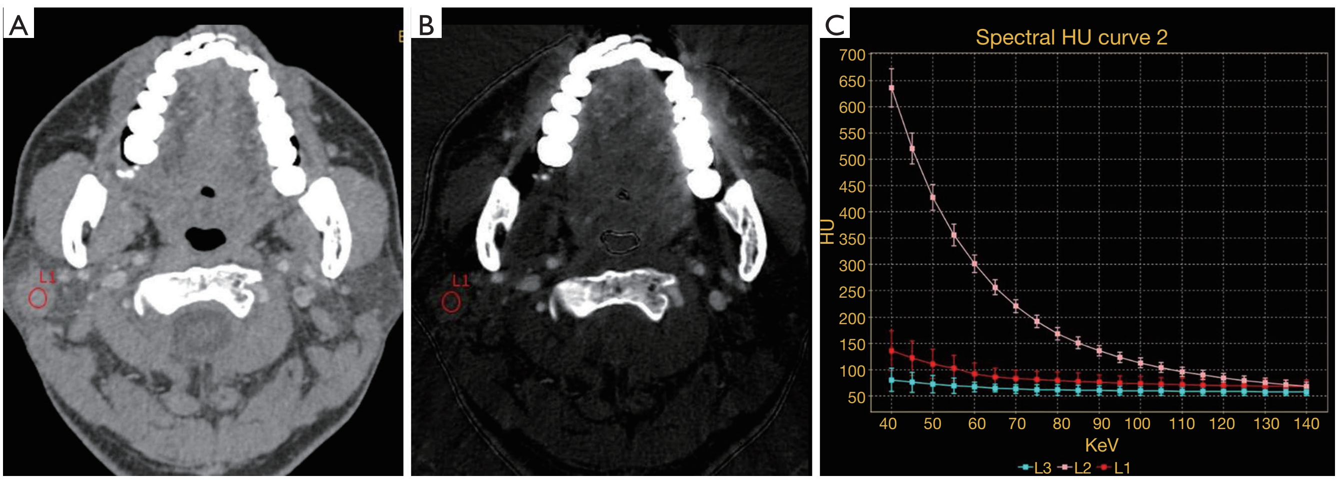

Figure 3 A 44-year-old male patient with MT (mucoepidermoid carcinomas). (A) Transverse 70 keV images after enhancement. The tumor locates in the right lobe of parotid gland with unclear border and moderate enhancement; (B) iodine-based material decomposition images and (C) the spectral HU curves are the tumor (L1, the red curve), CCA (L2, the pink curve) and sternocleidomastoid muscle (L3, the blue curve) respectively. The IC, NIC and λ_{HU} are 1.22 mg/mL, 0.16 and 1.45, respectively. MT, malignant tumor; CCA, common carotid arteries; IC, iodine concentration; NIC, normalized iodine concentration.

is very important for surgical procedures. The roles of CT or MRI in the differential diagnosis of parotid tumors have been discussed in previous studies (3-11). In several studies, multiphase contrast-enhanced CT/MR and CT/MR perfusion are the available imaging examination methods for the diagnosis of parotid tumors (5-11). In these studies, the sensitivities and specificities range from 74–86% and 79–92%, respectively (6,7,10,11). However, the radiation dose is higher when using CT perfusion and multiphase contrast-enhanced CT scan than conventional CT. And more time is needed when using multiphase contrast enhanced MR. Although traditional multiphase contrast-

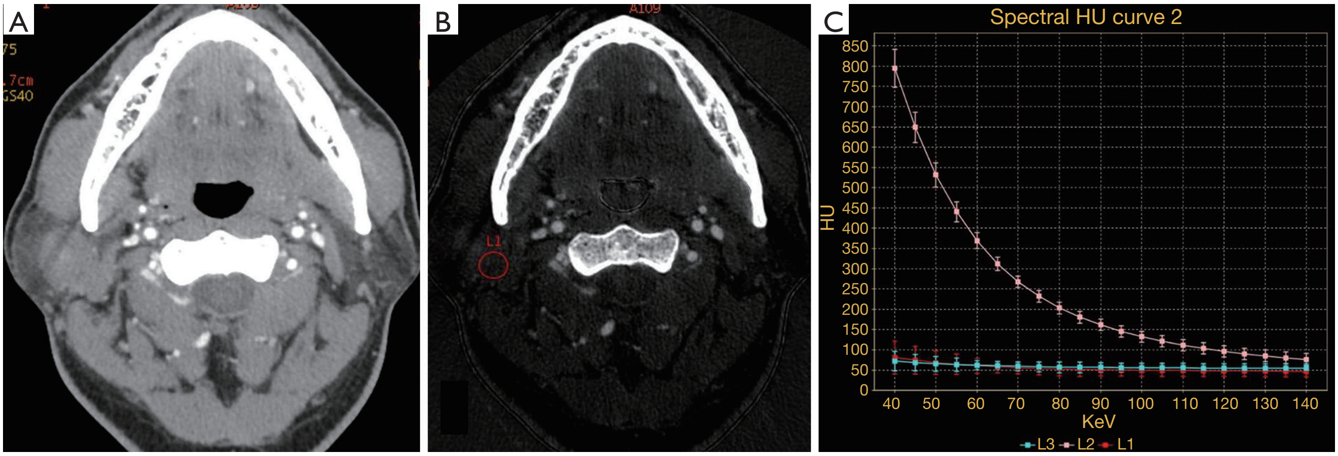

Figure 4 A 55-year-old male patient with PA. (A) Transverse 70 keV images after enhancement. The tumor locates in the right lobe of parotid gland with partial unclear border and mild enhancement; (B) iodine-based material decomposition images and (C) the spectral HU curves are the tumor (L1, the red curve), CCA (L2, the pink curve) and sternocleidomastoid muscle (L3, the blue curve) respectively. The IC, NIC and λ_{HU} are 0.64 mg/mL, 0.07 and 0.76, respectively. PA, pleomorphic adenoma; CCA, common carotid arteries; IC, iodine concentration; NIC, normalized iodine concentration.

Table 3 Thresholds, sensitivities, specificities and accuracy for differential diagnosis

Parameter	Threshold	Sen (%)	Spe (%)	Acc (%)	AUC	95% CI of AUC	
						Lower bound	Upper bound
IC_1	0.91 mg/mL	91.7	95.0	94.2	0.943	0.861	1.024
IC_2	1.46 mg/mL	91.7	89.3	90.4	0.844	0.689	0.998
NIC_{A1}	0.15	91.7	85.0	86.5	0.839	0.691	0.986
NIC_{A2}	0.20	95.8	85.7	90.4	0.826	0.658	0.993
λ_{HU1}	1.09	91.7	95.0	94.2	0.943	0.861	1.024
λ_{HU2}	1.72	91.7	89.3	90.4	0.849	0.695	1.003

IC_1, NIC_{A1} and λ_{HU1} are the thresholds value between groups of pleomorphic adenomas and malignant tumors; IC_2, NIC_{A2} and λ_{HU2} are the thresholds value between groups of Warthin tumors and malignant tumors; AUC, area under the curve; CI, confidence interval; IC, iodine concentration; NIC_A, normalized iodine concentration to common carotid artery.

enhanced CT/MR exhibits high sensitivity and specificity in the diagnosis of parotid gland tumors, it may occasionally lead to misdiagnosis when the features of the tumors are atypical or overlap.

DECT is a new and advanced form of CT in which simultaneous acquisitions are performed at two different energy spectrums, enabling material density and spectral HU curve beyond what is possible with conventional CT scans. A previous study showed that monochromatic images have increased the contrast-to-noise ratio (CNR) and reduced beam-hardening artifacts (22). Several researches revealed that the MD images and spectral HU curve showed differences between malignant and benign lesions (14-20). However, to our knowledge, the use of CT spectral imaging in the differential diagnosis of parotid gland tumors has not been reported. In the DECT imaging, we selected water and iodine as the basis pair for MD image presentation because iodine is the main ingredient of the contrast medium and the IC is a useful quantitative parameter that reflects the blood supply of lesions. Wang *et al.* (23) have shown that spectral CT imaging can accurately measure the IC of different proportions of iodine solution. Furthermore, the measured IC in lesions might be a useful quantitative parameter that directly reflects the blood flow

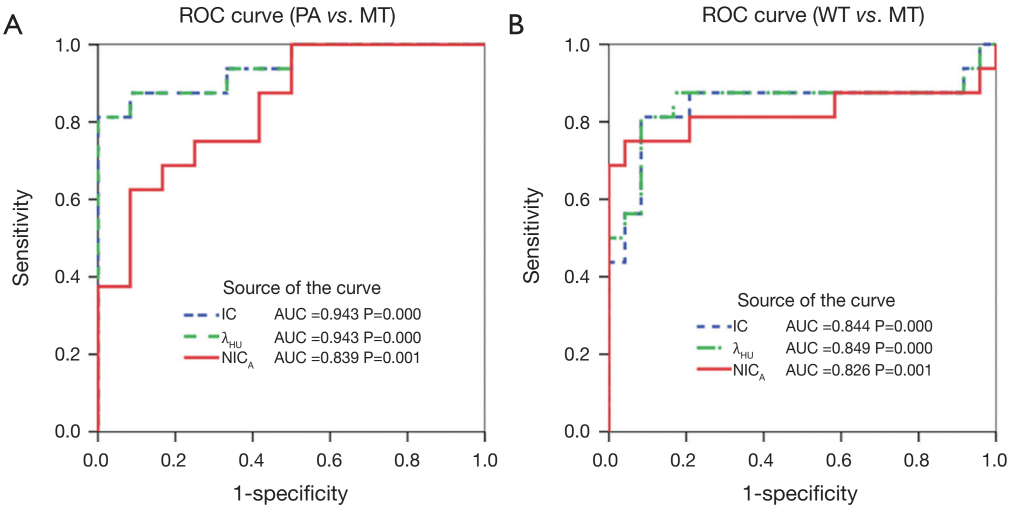

Figure 5 ROC curves for the IC, NIC_A, and λ_{HU} in differentiating (A) MT from PA and (B) MT from WT. The IC and λ_{HU} have higher diagnostic efficacies than NIC_A for the differential diagnosis. ROC, receiver operating characteristic; AUC, area under the curve; IC, iodine concentration; NIC_A, normalized iodine concentration to common carotid artery; PA, pleomorphic adenoma; MT, malignant tumor; WT, Warthin tumor.

and distribution in the intravascular and extracellular spaces.

On 70 keV images PA, WT and MT were not easily distinguished based on morphologic features (*Figures 2A,3A,4A*). Our study demonstrated that significant differences exist in IC, NIC and λ_{HU} among the PAs, WTs and MTs 3 groups, the IC, NIC and λ_{HU} of the WTs are higher than those of the MTs and PAs. This may be explained by the following reasons: WTs tend to be hypervascularized, and have an extensive capillary network and many leaky blood vessels (24,25). PAs are the most common benign tumors of the parotid glands, and are composed of epithelial, myoepithelial, and mesenchymal components (26). The mesenchymal components contain a lot of mucoid content and lack blood vessels, so the ICs in PAs were the lowest in the 3 groups. The growth of MTs is closely related to the neovascularization. Most MTs grow rapidly with peripheral vascular implantation to the tumor. This can lead to the high blood supply and high IC. However, most of the neovascularization were immature, so the ICs in the MTs were higher than those of PAs, while lower than those of WTs, consistent with the blood supply of the tumor. In our study, we found that two duct carcinomas showed high IC and λHU, probably because the solid and papillary areas of tumor have plenty of small blood vessels (27); hence, they showed hypervascular and higher IC.

In dual-energy spectral CT, the spectral HU curves can be automatically generated for given ROIs and reflect the dynamic change of measured CT values of ROIs against increasing keV values. It can directly reflect the difference between the substances. Previous studies have shown the usefulness of the slope of the spectral curve for the differential diagnosis of benign or malignant lesions (15,19,28-30). In our study, the λ_{HU} showed significant differences among the 3 groups. The λ_{HU} of WTs was the highest, followed by MTs, and the λ_{HU} of PAs was the lowest, which was consistent with IC, and also reflected the blood supply and internal composition of the tumor.

ROC curves analysis in our study revealed that the IC and the λ_{HU} had higher diagnostic efficacies than NIC_A for the differential diagnosis. IC and λ_{HU} had the same diagnostic efficacies. The IC can be measured directly and quickly in the ROI. Therefore, we recommend the use of IC as an applicable quantitative parameter in clinical practice.

It is worth mentioning that in this study we used the second generation of CT750HD and adopted a low tube current of 260 mA, which was far lower than the 550–600 mA in previous studies (31,32). And the application of single-phase enhanced scanning reduced the radiation dose to the patients.

There are several limitations to this study. First, this investigation just reflects our initial experience with a small number of patients. The accuracy of threshold values need to be confirmed by a large sample study in the future. Second, the sample size of the MT group was small and with different pathology types. Future studies will be needed for more different pathologies of malignancy. Third, this study also showed that the individuals in the WT group were more common in old men and multiple. Combining the IC and λ_{HU} with age and lesion number may help differentiate WTs in clinical practice. Hence, specific morphologic features are useful in determining parotid tumors. We believe that the combinations of morphological and quantitative evaluations of parotid gland tumors might improve the diagnostic accuracy, and further studies are needed in the future.

In conclusion, contrast-enhanced dual energy spectral CT imaging with quantitative parameters such as IC, NIC_A, and λ_{HU} may be a good and easy-to-use method for differential diagnosis in parotid gland tumors.

Acknowledgements

None.

Footnote

Conflicts of Interest: The authors have no conflicts of interest to declare.

Ethical Statement: The study was approved by the Ethics Committee of our hospital (No. NCC2016YZ-03) and all patients were provided with written informed consent.

References

1. Tian Z, Li L, Wang L, Hu Y, Li J. Salivary gland neoplasms in oral and maxillofacial regions: a 23-year retrospective study of 6982 cases in an eastern Chinese population. Int J Oral Maxillofac Surg 2010;39:235-42.
2. Patel KR, Scognamiglio T, Kutler DI, Kuhel WI, Gromis J, Phillips CD, Cohen MA.. Retrospective Assessment of the Utility of Imaging, Fine-Needle Aspiration Biopsy, and Intraoperative Frozen Section in the Management of Parotid Neoplasms: The Weill Cornell Medical College Experience. ORL J Otorhinolaryngol Relat Spec 2015;77:171-9.
3. Khalife A, Bakhshaee M, Davachi B, Mashhadi L, Khazaeni K. The Diagnostic Value of B-Mode Sonography in Differentiation of Malignant and Benign Tumors of the Parotid Gland. Iran J Otorhinolaryngol 2016;28:305-12.
4. Schick S, Steiner E, Gahleitner A, Böhm P, Helbich T, Ba-Ssalamah A, Mostbeck G. Differentiation of benign and malignant tumors of the parotid gland: value of pulsed Doppler and color Doppler sonography. Eur Radiol 1998;8:1462-7.
5. Hisatomi M, Asaumi J, Yanagi Y, Unetsubo T, Maki Y, Murakami J, Matsuzaki H, Honda Y, Konouchi H. . Diagnostic value of dynamic contrast-enhanced MRI in the salivary gland tumors. Oral Oncol 2007;43:940-7.
6. Lam PD, Kuribayashi A, Imaizumi A, Sakamoto J, Sumi Y, Yoshino N, Kurabayashi T. Differentiating benign and malignant salivary gland tumours: diagnostic criteria and the accuracy of dynamic contrast-enhanced MRI with high temporal resolution. Br J Radiol 2015;88:20140685.
7. Yabuuchi H, Matsuo Y, Kamitani T, Setoguchi T, Okafuji T, Soeda H, Sakai S, Hatakenaka M, Nakashima T, Oda Y, Honda H. Parotid gland tumors: can addition of diffusion-weighted MR imaging to dynamic contrast-enhanced MR imaging improve diagnostic accuracy in characterization? Radiology 2008;249:909-16.
8. Sumi M, Van Cauteren M, Sumi T, Obara M, Ichikawa Y, Nakamura T. Salivary gland tumors: use of intravoxel incoherent motion MR imaging for assessment of diffusion and perfusion for the differentiation of benign from malignant tumors. Radiology 2012;263:770-7.
9. Choi DS, Na DG, Byun HS, Ko YH, Kim CK, Cho JM, Lee HK. Salivary gland tumors: evaluation with two-phase helical CT. Radiology 2000;214:231-6.
10. Jin GQ, Su DK, Xie D, Zhao W, Liu LD, Zhu XN. Distinguishing benign from malignant parotid gland tumours: low-dose multi-phasic CT protocol with 5-minute delay. Eur Radiol 2011;21:1692-8.
11. Dong Y, Lei GW, Wang SW, Zheng SW, Ge Y, Wei FC. Diagnostic value of CT perfusion imaging for parotid neoplasms. Dentomaxillofac Radiol 2014;43:20130237.
12. Coursey CA, Nelson RC, Boll DT, Paulson EK, Ho LM, Neville AM, Marin D, Gupta RT, Schindera ST. Dual-energy multidetector CT: how does it work, what can it tell us, and when can we use it in abdominopelvic imaging? Radiographics 2010;30:1037-55.
13. Cui Y, Gao SY, Wang ZL, Li XT, Sun YS, Tang L, Zhang XP. Which should be the routine cross-sectional reconstruction mode in spectral CT imaging: monochromatic or polychromatic? Br J Radiol 2012;85:e887-90.
14. González-Pérez V, Arana E, Barrios M, Bartrés A, Cruz J, Montero R, González M, Deltoro C, Martínez-Pérez E, De Aguiar-Quevedo K, Arrarás M. Differentiation of benign and malignant lung lesions: Dual-Energy Computed Tomography findings. European Journal of

Radiology 2016;85:1765-72.
15. Hou WS, Wu HW, Yin Y, Cheng JJ, Zhang Q, Xu JR. Differentiation of lung cancers from inflammatory masses with dual-energy spectral CT imaging. Academic Radiology 2015;22:337-44.
16. Lv P, Lin XZ, Li J, Li W, Chen K. Differentiation of small hepatic hemangioma from small hepatocellular carcinoma: recently introduced spectral CT method. Radiology 2011;259:720-9.
17. Yu Y, Lin X, Chen K, Chai W, Hu S, Tang R, Zhang J, Cao L, Yan F. Hepatocellular carcinoma and focal nodular hyperplasia of the liver: differentiation with CT spectral imaging. Eur Radiol 2013;23:1660-8.
18. Yu Y, He N, Sun K, Lin X, Yan F, Chen K. Differentiating hepatocellular carcinoma from angiomyolipoma of the liver with CT spectral imaging: a preliminary study. Clin Radiol 2013;68:e491-7.
19. Yin Q, Zou X, Zai X, Wu Z, Wu Q, Jiang X, Chen H, Miao F. Pancreatic ductal adenocarcinoma and chronic mass-forming pancreatitis: Differentiation with dual-energy MDCT in spectral imaging mode. Eur J Radiol 2015;84:2470-6.
20. Li M, Zheng X, Li J, Yang Y, Lu C, Xu H, Yu B, Xiao L, Zhang G, Hua Y. Dual-energy computed tomography imaging of thyroid nodule specimens: comparison with pathologic findings. Invest Radiol 2012;47:58-64.
21. Al Ajmi E, Forghani B, Reinhold C, Bayat M, Forghani R. Spectral multi-energy CT texture analysis with machine learning for tissue classification: an investigation using classification of benign parotid tumours as a testing paradigm. Eur Radiol 2018;28:2604-11.
22. Lin XZ, Miao F, Li JY, Dong HP, Shen Y, Chen KM. High-definition CT Gemstone spectral imaging of the brain: initial results of selecting optimal monochromatic image for beam-hardening artifacts and image noise reduction. J Comput Assist Tomogr 2011;35:294-7.
23. Wang L, Liu B, Wu XW, Wang J, Zhou Y, Wang WQ, Zhu XH, Yu YQ, Li XH, Zhang S, Shen Y. Correlation between CT attenuation value and iodine concentration in vitro: Discrepancy between gemstone spectral imaging on single-source dual-energy CT and traditional polychromatic X-ray imaging. J Med Imaging Radiat Oncol 2012;56:379-83.
24. Woo SH, Choi DS, Kim JP, Park JJ, Joo YH, Chung PS, Kim BY, Ko YH, Jeong HS, Kim HJ. Two-phase computed tomography study of warthin tumor of parotid gland: differentiation from other parotid gland tumors and its pathologic explanation. J Comput Assist Tomogr 2013;37:518-24.
25. Ikeda M, Motoori K, Hanazawa T, Nagai Y, Yamamoto S, Ueda T, Funatsu H, Ito H. Warthin tumor of the parotid gland: diagnostic value of MR imaging with histopathologic correlation. AJNR Am J Neuroradiol 2004;25:1256-62.
26. Lopes ML, Barroso KM, Henriques ÁC, Dos Santos JN, Martins MD, de Souza LB. Pleomorphic adenomas of the salivary glands: retrospective multicentric study of 130 cases with emphasis on histopathological features. Eur Arch Otorhinolaryngol 2017;274:543-51.
27. Fenesan DI, Lenghel M, Băciuţ G, Văcăraş S, Botar-Jid C, Vasilescu D, Dudea SM. Ultrasound and CT imaging features in a patient with salivary duct carcinoma of the parotid gland: a case report with literature review. Med Ultrason 2015;17:119-22.
28. Srinivasan A, Parker RA, Manjunathan A, Ibrahim M, Shah GV, Mukherji SK. Differentiation of benign and malignant neck pathologies: preliminary experience using spectral computed tomography. J Comput Assist Tomogr 2013;37:666-72.
29. Wu LM, Li YL, Yin YH, Hou GQ, Zhu R, Hua XL, Xu JR, Chen ZA. Usefulness of dual-energy computed tomography imaging in the differential diagnosis of sellar meningiomas and pituitary adenomas: preliminary report. PLoS ONE 2014;9:e90658.
30. Yang L, Luo D, Li L, Zhao Y, Lin M, Guo W, Zhou C. Differentiation of malignant cervical lymphadenopathy by dual-energy CT: a preliminary analysis. Sci Rep 2016;6:31020.
31. Liu X, Ouyang D, Li H, Zhang R, Lv Y, Yang A, Xie C. Papillary thyroid cancer: dual-energy spectral CT quantitative parameters for preoperative diagnosis of metastasis to the cervical lymph nodes. Radiology 2015;275:167-76.
32. Li HW, Wu XW, Liu B, Liu WD, Gao N. Clinical values of of gemstone spectral CT in diagnosing thyroid disease. J Xray Sci Technol 2015;23:45-56.

Cite this article as: Li L, Zhao Y, Luo D, Yang L, Hu L, Zhao X, Wang Y, Liu W. Diagnostic value of single-source dual-energy spectral computed tomography in differentiating parotid gland tumors: initial results. Quant Imaging Med Surg 2018;8(6):588-596. doi: 10.21037/qims.2018.07.07